NUMERICAL AND EXPERIMENTAL EVALUATION OF A LHTES SYSTEM USING PCMS UNDER DIFFERENT CONFIGURATIONS OF NOZZLE AND SHELL INTEGRATED WITH SOLAR EVACUATED TUBE COLLECTORS

Ali Amjed Saeed1*,
Audai Hussein Al-Abbas 2,
Hani Mizhir Magid 3
1 Al-Furat Al-Awsat Technical University,
Al-Mussaib Technical College, Babylon 51006, Iraq
2 Al-Furat Al-Awsat Technical University,
Al-Mussaib Technical College, Babylon 51006, Iraq
3 Al-Furat Al-Awsat Technical University,
Al-Mussaib Technical College, Babylon 51006, Iraq
Corresponding Author Email: aliamjad.iq1996@gmail.com

Abstract

To improve the performance of solar energy, this study provides a novel shell and nozzle tube LHTES across two different geometries fins (tilted longitudinal and solid annular) and an investigation of the melting patterns of two types of commercial PCMs (lauric acid and paraffin wax). During the melting (charging) process, numerical simulations were conducted and compared with experimental observations for the bare nozzle pipe and finned tube configurations placed vertically. The average temperature and profile liquid fraction of the PCM through the melting operation in all model setups are employed for validation tests. The evaluation of the liquid fraction revealed that the numerical findings exhibited remarkable qualitative concordance with the experiment in all analyzed cases. The results demonstrate that annular fins and tilted longitudinal designs are seen to enhance the melting rate and temperature distribution by developing heat transfer, which shows an important benefit with an approximate decrease in total melting times of 38.3% and 12.98%. Moreover, three various inlet HTF temperatures (70 °C, 75 °C, and 80 °C) and flow rates (3, 5, and 7 L/min) of the HTF were evaluated during the melting process in PCM. A 5°C rise in the HTF temperature significantly impacted all cases; however, an especially affected reference case enhanced the overall melting time by about 34.97% and 21.32%. The largest decrease in total melting time was around 8.5% when the flow rate was raised from 3 to 7 L/Min. Therefore, the role of the HTF flow rate is less prominent; it can be considered marginal.

Keywords: Latent heat thermal energy storage (LHTES), Phase change material (paraffin wax and lauric acid), Tube shapes, Layout fins, melt fraction, and Heat transfer fluid (HTF).

Introduction

Solar energy is an alternative to the global problems of high energy carbon emissions and consumption. However, its use could be improved by consistent energy supply and demand caused by its random fluctuations and intermittent availability [1], [2]. Thermochemical, sensible, and

latent energy storage are the three basic categories of thermal energy storage (TES) applied to solar power utilization and demand-shifting [3]. It offers numerous benefits, including high energy density and extensive storage capacity throughout the charging /discharging operations within a limited temperature range. LHTES is an Approach often employed in solar system thermal storage devices [4]. Furthermore, PCM methods techniques have the option to be implemented in other fields, including heat loss restoration, Cooling/ heating roofs, walls, floors, and ventilated residential buildings [5]–[7]. Air conditioning systems [8], PV-Pannal [9], etc.

The thermal effectiveness of LHTES is predominantly limited by two variables: the geometric structure of the heat exchanger [10] and the PCM's weak thermal conductivity [11]. Combining a shell-and-tube heat exchanger with PCMs is frequently utilized in manufacturing applications containing LHTES. In conventional heat transfer devices, the shell and tube involve PCMs; the tube pumps a high- or low-temperature HTF, and the shell side is occupied with PCMs for energy charging or discharging processes [12].To enhance the energy storage performance of a shell-and-tube heat exchanger, modify and augment attributes that previous studies have demonstrated, such as the hydraulics diameter of the tube radius ratio [13], [14], Modified geometry of the tube [15], mass flow rate [16] inlet HTF temperature [17] and tube eccentricity [18]. The diameter of the tube and the inlet HTF temperature have a more significant influence on the heat transfer rate than the tube thickness and inlet mass flow rate [19].

Moreover, the thermal performance might be influenced by several other parameters, like the design, layout, inclination angle, and structure of the external shell of the PCM [20], regarding the natural characteristics of PCMs with weak thermal conductivity. Innovative PCMs have been created and validated to enhance the energy storage performance of a shell-and-tube heat exchange system by developing technology by incorporating nanoparticles [21], [22], Porous structure [23], and nanoparticles metal foam hybrids [24] And fin foam hybrids [25], [26] Among the combination mentioned above of heat transfer enhancement strategies, conduct fins are considered one of the most incredible viable approaches to defeat difficulty due to their high enhancement of the heat transfer ratio, simple structure, cheap cost, and ease of manufacture and operation [10].

Numerous studies have been conducted to develop complicated fin structures to enhance TES tube design. The longitude [27], annular [28], spiral fin [29], Plate Fin [30], hierarchical fins [31], spiderweb-like fins [32], Bionic topology of fins [33], bifurcated and straight fins [34]. The annular or circular fins are a typical structure for efficiently improving the heat transfer of PCM in a shell-and-tube heat exchange system. A circular fin design was adopted in the PCM domain and non-uniform position, resulting in a significant 70% decrease in the total melting time [35].

The study Yang et al. conducted in 2020 [36] Theoretical and experimental research to create a design plan for annular fins with regular and irregular spacing. The purpose was to analyze the melting behavior and discover how the fins' pitch and position affect the melting fraction's thermal perfor-mance and enhancement in a vertical thermal storage unit with uniform temperatures. The findings indicated an 84.7% enhancement in the melting process when an irregular pattern distance was used, as opposed to a regular form. Due to the impact that irregular fins disturb the PCMs and make them heterogeneous. Tiari et al. 2021 [37] connected the H.T.F. tube to the annular fins. The fins applied according to the system's thickness are classified into two separate groups: ten of 1.5 mm and twenty of 0.794 mm. Also, it has a circular fin with uniform length and diameter and is installed on the central tube. The comparison process was carried out with a tube that does not

have fins to measure the effectiveness of the annular. The result indicates that the length with extended fins at the base of the pipe overall decreased time by 73.7%. Moreover, the best case among the optimal configurations studied for time solidification reduced in uniform length with 20 fins was 79.2%. According to the overall time reduction, it was 76.3% in charging and discharging operations. The research examined how different length-width ratios (AR = 0.5–1–1.5 and 2) of horizontal shells accompanied by a T-shaped geometric final destination impact their performance.

Karami and Kamkari 2020 [38] the experimental two different types of solid and perforated annular finned TES tubes. The study focused on analyzing the created TES tube coupled melting processes. Their results indicated that local natural convection currents were the primary influence on the development of the melting front. Pu et al. 2020 [39]. focused on maximizing the arrangement of circular fins to increase the melting rate for thermal applications. An ANSYS-Fluent-based computational prototype was const-ructed, and simulations were conducted to examine the imp-acts of fin altitude and pitch on the melting rate. After analyzing the numbers, researchers suggested applying a dimensionless height of 0.642 for circular fins.

Dai et al. 2024 [40] guide its optimal configurations. An alternative design eccentric may improve the melting operation occurring at the bottom regions, raising the energy storage rate and melting quality despite reducing temperature inconsistencies. The perfect concentric distance for the T-shaped fin contributes to a 42.50% increase in melting efficiency compared to the concentric construction. AR of 0.5 is the reference case for comparison, and the melting time dropped by 34.48%. Nevertheless, their enhancement growth dropped progressively to 19.23%, 18.18%, and 10.0%, respectively. The locations of the rotation angle of the fins are critical because they reach the farthest region in the shell and affect the buoyant force PCM. Al-Mudhafar et al. 2021 [41] Heat exchangers equipped with visible fins and six T-shaped fins are considered the most significant advancements for expediting the melting process. Adding six tree fins and six longitudinal fins resulted in a 33% decrease in the time needed to achieve total melting compared to exclusively longitudinal fins. The shell without fins experienced 15% total melting of the PCM after 6 hours, but the shell with tee geometry resulted in PCM melting in around 3.5 hours.

In Khan and Khan's study conducted in 2020 [42], the researchers found that the arrangement and orientation of the fins have a crucial influence, and the dimensions (length, width, thickness, and thermal diffusion) and details of the fins are studied for the optimal placement method. This study attempts to determine and evaluate the influence of adjustments in the inclination angle on thermal performance. A test structure is utilized to construct a horizontal LHTES in a Y-fin configuration inside a copper tube with an isothermal steel shell instead of λ-fins. The temperatures are distributed uniformly at five distinct angular points (90°, 75°, 60°, 45°, and 30°) from the central point of the longitudinal circumference. The configuration employs stearic acids PCMs to store thermal energy. The result showed that design Y-fin offers a shorter charging time of 50.7% and enhanced capacity energy storage by about 10%. The fulfilled Copper shell reduced the process melting duration time by 32.4%. Compared to the standard format, λ-fins Mahdi, Hasan, et al. 2019 [43] Compare a tube equipped with longitudinal fins and a tube without fins. The liquid fraction processes were constantly tracked, and the investigation demonstrated an excellent degree of agreement in all parameters, with a maximum error rate of no more than 3.6%. The findings indicate that including fins decreases the melting process's average duration by 50%. The non-

finned tubes exhibit a higher melting rate when positioned horizontally or vertically. Conversely, it was discovered that orientation had little effect on the melting process when using finned tubes. The research was undertaken by Benmoussa et al. in 2017 [44] aimed to investigate the thermal behavior and energy storage capacity of (LHESU) by applying two different (PCMs1 accompanied by a melting point of 323 K and PCMs2 with a melting point of 333 K). The study also examined the effect of the temperature inlet of the H.T.F. at a constant flow rate of 0.03 m/s on the time required for complete melting in a shell and tube configuration. Research results indicate that raising the temperature of the fluid that enters has a considerable positive impact on the overall melting time in PCMs1, which is faster than in PCMs2. An increase in the initial H.T.F temperature from 338 K to 353 K in PCMs2 resulted in a decrease of the melting time from 1870 s to 490 s, corresponding to a decrease of 78.3%. The time it required for PCMs1 to melt dropped from 530 seconds to 270 seconds, reducing 49.1%.

The literature survey evaluation above demonstrates that previous investigations on the LHTES unit mainly concentrated on improving the fin geometric and structural design constituting the LHTES configuration. The numerical models were first verified by comparing them to quantitative and qualitative experimental data. This comprehensive research presents a numerical investigation accomplished utilizing a CFD method in vertical designs with different fin geometrical parameters (non-finned Nozzle tube, Nozzle with tilted longitudinal fins, and nozzle solid annular fins) process under various operating conditions to Investigate the influence of inlet HTF temperature, and inlet HTF flow rate on melting fraction profiles, patterns temperature distrib-ution, and thermal storage performance. The comparison of the findings with experimental values and a previous study in a shell-and-tube LHSU validates the CFD's reliability. The novel design of the tube and fins provides a structure for developing optimum design methodologies for practical applications.

2-Numerical simulation and Modeling

SOLIDWORKS 2020 generates a straightforward and comp-lex engineering design for the three-dimensional testing model, as depicted in **Figure 1 a**. A numerical design was built using CFD methodologies ANSYS Flow Fluent R.22 was utilized for this purpose. Three distinct storage concepts exist to minimize the need for extensive physical experiments to gain valuable insights into this system **Figure 1 b**. The enthalpy-porosity approach was used to model the PCM in the LHSU system. To analyze the flow of turbulent water (HTF), a standard turbulence model, specifically the k-epsilon model, was used. The numerical analysis included three computational reports: report 1 for the HTF flow, report 2 for the average temperature of the HTF pipe with fins, and, ultimately, report 3 for the average melting PCM. The thermal properties of the material geometry utilized were considered throughout the calculation to enhance the simulation's precision.
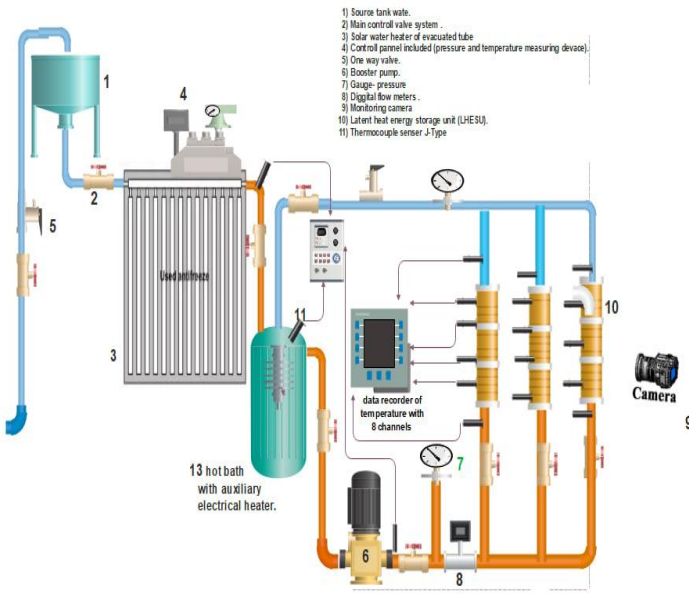
Figure 1 b-3D Model of Nozzle and shell, Model of Tilted longitudinal fins, and Model of new design annular fins
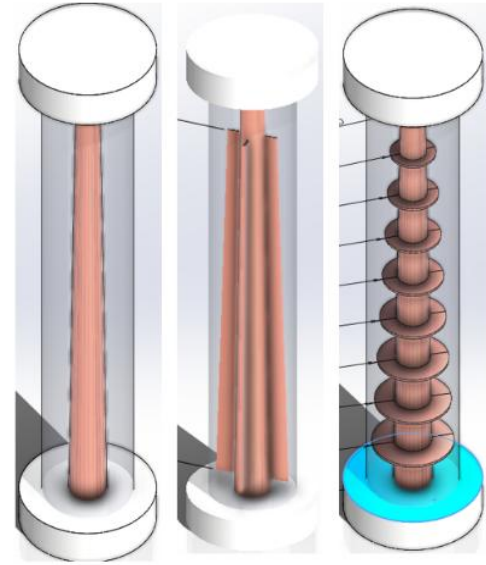
Figure b a. 2D Schematic diagram. (1) Source tank water (2) Main control valve system (3) Evacuated tube solar collector (4) control panel included (pressure and temperature measuring devices) (5) One-way valve (6) booster pump (7) Gauge-pressure (8) digital flow meters. (9) Monitoring camera (10) Heat exchangers (11) Thermocouple sensor J-Type

The simulation process used the following assumptions and boundary conditions:

1. The PCM and geometry structure's initialization temperat-ure for the melting process was specified at 25 °C. Conseq-uently, the experimental test was conducted at a room temperature of 25 ◦C. Each test was performed when the LHTES system had been sufficiently cooled to match the ambient temperature.

2. Asymmetrical boundaries constraint was enforced on the center straight cross portion of the units. The exterior surface of the container LHTSU was assumed to be banded and, consequently, temperature isolated.

3. The water's physical characteristics were assumed to have constant
values, as shown in **Table 1**.

4- The characteristics of the PCM remained constant. The liquid PCM undergoes current natural convection, as previously discussed, due to variations in its density at various temperatures. The Boussinesq approach was applied.

$$\rho = \rho_o\{1 - \beta(T - T_O)\}\ldots (1)$$

5. The model's governing equations could possibly be briefly stated as follows:

- Continuity equation

$$\nabla \vec{v} = 0\ldots (2)$$

- The momentum equations

$$\rho \ \frac{\partial \vec{v}}{\partial t} + \rho \ (\nabla \vec{v})\vec{V} = -\nabla P + \mu\nabla^2\vec{V} + \rho\beta\vec{g}(T - T_O) + \vec{S}\ldots (3)$$

- Conservation of the energy equation

$$\frac{\partial}{\partial t}(\rho H) + \nabla.\left(\rho\vec{V}H\right) = \nabla.(K\nabla T)\ldots (4)$$

Regarding the equations mentioned previously, $\rho, \vec{v}, \vec{V}, \beta, P, t, T_O, \vec{g}, \mu$ and K are density, velocity, thermal expansion coefficient, pressure, time, temperature of reference, acceleration

due to gravity, dynamic viscosity, and thermal conductivity, respectively. The enthalpy-porosity concept considers the mushy zone to be a porous medium. The porosity of each element is assumed to have a value equivalent to the fraction of liquid available in that ingredient. The term S is momentum sink, produced by the decreased porosity in the mushy zone:

$$\vec{S} = \frac{(1-f)^2}{(f^3+\alpha^3)}\vec{V} * A_{meshy} \ldots (5)$$

The factor A_{meshy} represents a fixed value of the mushy area. The influence of multiple values of A_{meshy} $(10^4, 10^5, 10^6, and\,10^7)$ The period of time necessary to complete the melting of PCM was studied. The mushy factor has little impact on the time taken to melt the PCM until the value is exceeded (10^5) .The research selected an established value of A_{meshy} at 10^5, $Kg/m^3.s$ resulting in excellent agreement among the numerical and experimental results. This correlates with the research that has already been published [43] .

At last, H indicates an overall enthalpy consisting of sensible heat and latent aspects.
H = h + Δ H … (6)
Where the specific enthalpy
$$h = h_0 + \int_{T_0}^{T} C_p dt \ldots (7)$$
The enthalpy change resulting from the phase transition may be expressed in the PCM's latent heat:
Δ H = fL … (8)
In this context, L represents the latent heat of the PCM, whereas f denotes the liquid percentage, which ranges from 0 to 1, as shown by:

$f = 0,$ at $T < T_{solidus}$ solid

$f = \frac{T - T_{solidus}}{T_{liquidus} - T_{solidus}}$, at $T_{liquidus} < T < T_{solidus}$ mushy

$f = 1,$ at $T > T_{liquidus}$ liquid

To improve the dependability of the integration, under-relaxation parameters are applied: 0.45,1,0.7, 0.987, and 1; the variables considered were pressure, momentum, energy, liquid fraction, and turbulence viscosity, respectively. The workbench (ANSYS) was used to develop the geometry mesh.

Complex meshes were created for all models in the LHTSU. A fine mesh was used across the interfaces to ensure that the cell sides matched correctly and to prevent any overlap between regions of the cells. The average element grade and skewness scores were 0.85,0.815, and 0.1, respectively. Several tests were conducted utilizing all the model's finned tubes to identify results affected by the mesh size and time step.

Table 1. The thermophysical characteristics of lauric acid, paraffin wax, water, and copper pipes.

property	Unit	PCM1 (Lauric acid)	PCM2 (Paraffin wax)	Copper
Rang Melting point	°C	41-44	50-54	N/A
Density liquid/solid	Kg /m^3	775/880	750/890	8900
Thermal conductivity	W//m . K	0.3	0.22	390
Specific heat capacity	KJ/Kg. K	2.15	2.14	0.380
Latent heat of fusion	KJ/Kg	174	186	N/A
Thermal expansion	$1/K$	0.0006	0.0008	N/A
viscosity	$Pa.s$	0.026	0.009	N/A

Figure 2 demonstrates the correlation between the number of cells and the progression of the PCM melting in the annular finned pipe LHSU. Three varying quantities of cells were analyzed on those mentioned above. The consequence of the total cell counts on the PCM percentage liquid fraction is minimal as the total number of cells increases from (824504, 944025, and 1170125).

Figure 3 illustrates the influence of the time step on the PCM's liquid fraction percentage through a process of melting in the finned (LHSU). The chart shows that the impact of time steps was insignificant when dropping from 0.3, 0.1, and 0.05 seconds. Therefore, after a thorough investigation, a time value of 0.1 s was chosen for non-finned tube LHSU to save processing time. The values published previously [43] are in agreement with these results. The solution's convergence is evaluated at every time step, with the criteria for convergence set at (10^-4, 10^-5, and 10^-7) for the remaining variables of the continuity, velocity, and energy equations, respectively. The time requirement to finish a simulation of all finned and bare pipe structure cases was 23 days. The CFD simulation was conducted on an efficient Laptop equipped with an i9 core processor running at 2.3 GHz and 16 GB.
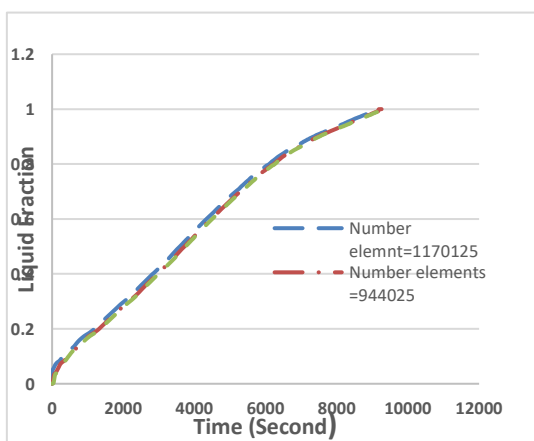

Figure 2: the liquid fraction percent against Mesh elements number of the present investigation.
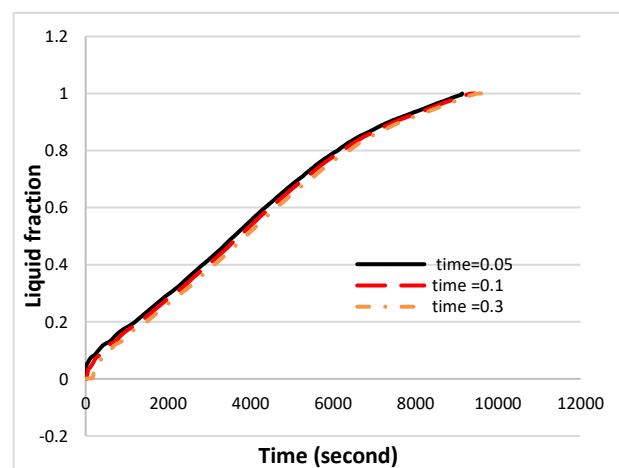

Figure 3: The impact of altering the time step on the progression of the average liquid fraction of the PCM was studied using a mesh including 944025 elements.

3.1 Thermophysical characteristics of PCMs

Maintaining the stability of thermophysical characteristics is crucial for PCM to prevent thermal failure throughout the power melting/solidification mechanism. Based on these requirements, two types of high-quality PCM (lauric acid and paraffin wax) with different properties were provided to study the effect of physical properties, compare them, and find the optimal one that meets the criterion of the shortest melting time. The current work measured the Different Scanning calorimetry (DSC), which was applied to identify the thermos-physical characteristics of PCMs (lauric acid and paraffin wax) specific experimental methods, as demonstrated in **Figure 4**. The DSC conducted thermal conductivity testing, specific heat capacity, and latent heat and determined the PCM's range of melting temperature points. However, the density of PCM varied depending on the temperature. The thermal expansion coefficient and the PCM's viscosity were acquired from published sources. **Table 1** Observa-tion of thermo-physical characteristics was assumed independent of temperature and properties of copper tubes, working fluid (water), lauric acid, and paraffin waxes.
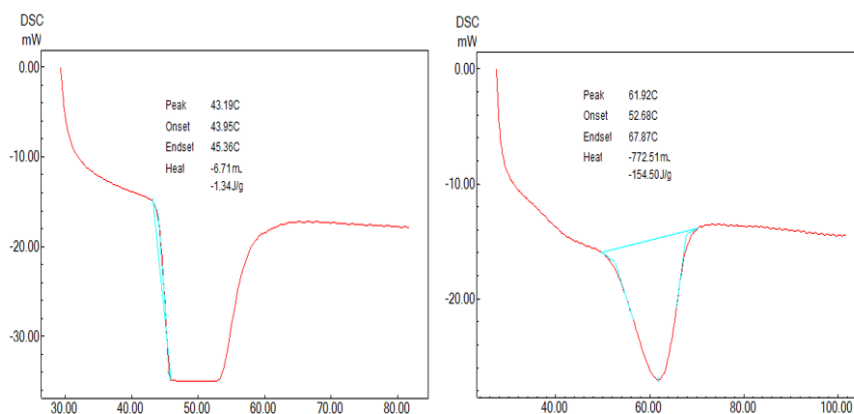

Figure 4: The result of the DSC melting enthalpy curve was produced for the commercially available PCMs (Paraffin waxes and Lauric acid) used

3.2 Experimental setup

An experimental arrangement was devised and constructed to examine the properties of the PCM melting operation in a nozzle tube and shell-TES unit in three different configurations: non-finned Nozzle tube, Nozzle with tilted longitudinal fins, and Nozzle pyramid annular fins. The experimental system test apparatus **Fig 5** consisted essentially of three components:(a) the component for generating the HTF, (b) the testing component, and(c) the Data collection component.
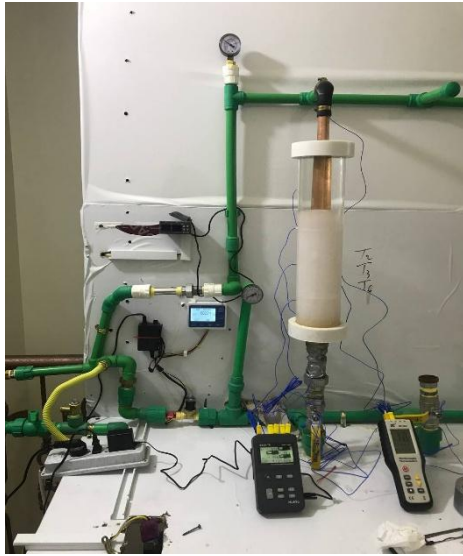
Figure 5: Photographic view of the present system

Figure 6 a: Evacuated tube solar collector

Figure 6 b: Hot bath with an auxiliary electrical

B) The testing components

The primary component of that part was a shell-and-nozzle tube TES unit. The extreme temperatures of HTF streamed during the bottom nozzle while the PCM occupied the shell entirely, as observed in the figure. The copper nozzle was fabricated with input and output diameters of 39 mm to 24 mm, respectively, and a thickness of 2 mm; a pipe was positioned in the center of the cylinder shell. The fins maintained a uniform thickness of 3 mm.

Fig 7 shows the distribution in all models (case reference, tilted longitudinal fins, and the solid annular) with varying dimensions on the external surface of the tube. The shells were designed as concentric circular transparent acrylic Perspex tubes, which provide visualization of the fusion process. The shell's dimension has an internal diameter of 90 mm and an external diameter of 100 mm, with the height in the reference case being 450 mm and, in the other situations, 484 mm, to ensure that the PCM mass remains constant in all configurations for comparison. The pipes were attached to the internal shell by two flange isolators established from Styrofoam for each unit with a thickness of 35 mm. Special attention was devoted to monitoring the outside temperatures of the thermal insulation layers' exterior surface and the surrounding atmosphere. It is essential to mention that the PCM's content capacity was decreased to approximately accommodate the 10% increase in the expansion volume of paraffin after it melts. The heat loss can be determined by applying Fourier's thermal conduction equations.
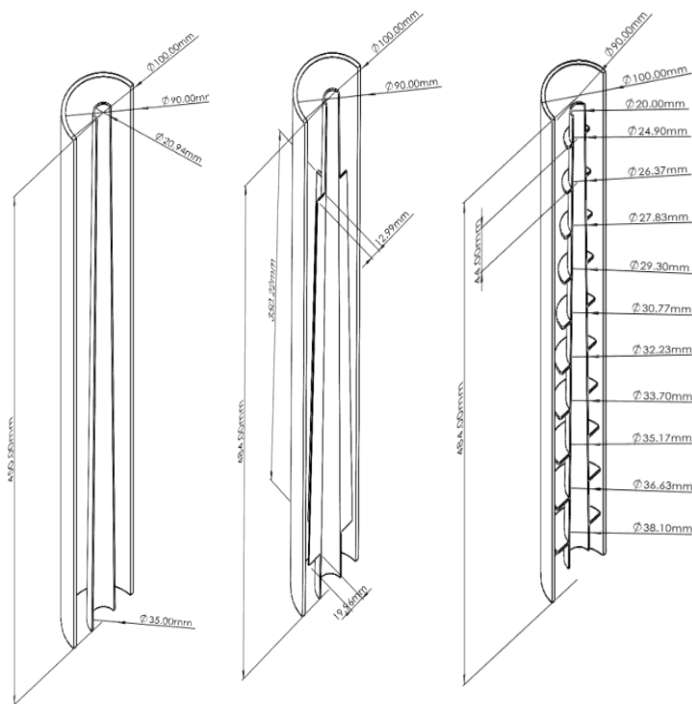
Figure 7: illustrates the dimensions of all comp-onents in the test section (all measurements are in mm).
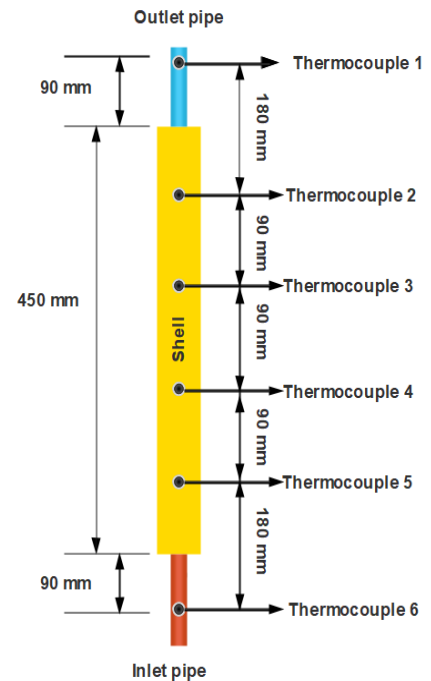
Figure 8: Thermocouples distribution along the test section.

C) The data collection component

During this component, the evaluation was conducted to analyze the thermal response, and the performance of the vertical TES system that had previously been constructed was assessed. The thermocouple was wiring strands of injector 1.2 mm in diameter, length 3m, and capable of evaluating temperatures ranging from -40 ◦C to 400 ◦C, each with an average uncertainty of ± 0.2 °C. Six K-type thermocouples were used along each unit. Four thermo-couples were installed on the inner surface of the shell inside the PCM, while the remaining two measured the HTF temperatures at the inlet and exit sites, as shown in **Fig 8**. The thermocouples were directly linked to a portable data logger multichannel module HUATO S220-T8, with an acquisition resolution of 0.1 % selected for data collection. A portable thermometer device, precisely the Moodle Hti HT-9815 comprehension, was employed to predict the temperatures of both solar and electric heaters in the HTF production units

3.3 Experimental procedure

1. To successfully install and verify the test properties of the PCM, a 5mg sample of (lauric acid and paraffin) was set in a covered steel pan and warmed to 90 % for 30 minutes to remove any temperature memory effect. The test gradually increases the heating rate of 5 °C/min within the ambient to 90°C. The heated material is frozen by exposing it to a 100 ml/min flow rate of liquid nitrogen. The melting/ solidification points sketch a path with the maximum gradient from the spot. The peak area is numerically integrated to determine the latent heat. The KD2 Pro is a portable device designed for sensing thermal features in single-prop

detectors that are used to quantify by the dual scale devices to measure thermal conductivity, volumetric specific heat capacity, resistivity, and diffusivity.

2. -To accomplish the design and installation of the test rig, the HTF was pumped into the constant-temperature tank and circulated throughout the experimental rig to avoid possible leaks. Before each test, PCM was heated until it reached its melting point using a Wax melting machine. It was then carefully poured into the concentric cylinders to prevent the formation of bubbles or splashing. The first empirical measurement was cautiously conducted after a suitable time for the complete solidification of PCM. Furthermore, verify once the surface of the solidified PCM has undergone artificial polishing to achieve a smooth and even level.

3. Once the experimental setup is adequately prepared, a thermostat is connected to the bath tank to circulate the water inside the tank via the main valve.

4. If the tank's water temperature reached the desired temperature and remained stable for a particular duration, the valve inlet and outlet were activated, while the control valve was employed for calibration to deliver a flow rate that closely matched the expected value.

5. The information acquisition system recorded tempe-rature values obtained from temperature sensors and flow rate values determined by a digital flowmeter at 30-second intervals.

3.4 The Evaluation of Uncertainty

The analytical reliability of each device and sensor employed in the test work is confirmed. The accurate measurements of the equipment's relative and absolute accuracies were obtained from their information sheets. Undoubtedly, most of the determination mistakes may be attributed to inaccuracies in the recorded values. Therefore, the discrep-ancy in the acquired outcomes must be determined. The Kline and McClintock approach [45] is applied in this domain. Consider the value of R as a function that the indep-endent variables $(X_1, X_2, ... X_n)$.

$$R = (X_1, X_2, X_3 ... ... X_n) ... (1)$$

Considering a few fluctuations in the variables, the relationship can be represented in a linear format:

$$\delta R = \frac{\partial R}{\partial X_1} \delta X_1 + \frac{\partial R}{\partial X_2} \delta X_2 + \frac{\partial R}{\partial X_3} \delta X_3 + ... + \frac{\partial R}{\partial X_n} \delta X_n ... (2)$$

Hence, the magnitude of uncertainty (W) in the outcome may be represented as

$$W_R = \left[\left(\frac{\partial R}{\partial X_1} W_1\right)^2 + \left(\frac{\partial R}{\partial X_2} W_2\right)^2 + \left(\frac{\partial R}{\partial X_3} W_3\right)^2 + \cdots + \left(\frac{\partial R}{\partial X_n} W_n\right)^2 \right]^{\frac{1}{2}} ... (3)$$

Minimizing equation (2) by R is significantly simplified and made non-dimensional.

$$\left(\frac{W_R}{R}\right)^2 = \left(\frac{\partial R}{\partial X_1} \frac{W_1}{R}\right)^2 + \left(\frac{\partial R}{\partial X_2} \frac{W_2}{R}\right)^2 + \left(\frac{\partial R}{\partial X_3} \frac{W_3}{R}\right)^2 + \cdots + \left(\frac{\partial R}{\partial X_n} \frac{W_n}{R}\right)^2 ... (4)$$

Therefore, the possibility of experimentation errors resulting from including the variables in question, according to Eqs. (2) and (3), the highest uncertainty values for the apparatus, (Data logger (S220-T8), Thermometers thermocouple (HT-9815), K-type thermocouple (TP-02 A), Flow mete YF-B2 are $\pm 0.1 \degree C$, $\pm 0.1 \degree C \pm 0.1 \degree C$, and $\pm 0.5 \degree C$, respectively.

4.The Results and Discussions

4.1- Numerical Models Evaluation

Experimental procedures were carried out as outlined in Section 3.3 above to ensure precision and certainty in the numerical model of the LHTES. The research focused on two specific aspects: the temperature distribution, which was validated using thermocouples data measurements, and the percentage of the liquid fraction of the PCM throughout the time melting process. A comparison between the experimental test and CFD results for different layout geometry, with variation in inlet HTF temperature over time and in various flow rates during thermal charging processes. General results indicate an excellent percentage of agreement between the experimental and CFD studies. The accuracy decreases as the charging time increases due to the rising loss rates attributed to the outside conditions in practical application tests. The evaluating ratio for paraffin wax has declined compared to Lauric acid's more accurate validation number. The annular fin charge process shows the most significant accuracy percentage, with Lauric acid at an inlet temperature of 80 °C and a flow rate of 7L/MIN, achieving an estimated value of 96%. The minimum accuracy validity ratio in the reference model applying at an inlet temperature of 70 °C and a flow rate of 3 L/min is 91%. The general trend is that increasing the inlet temperature and flow rate raises the accuracy ratio. **Figure 9 and 10** Indicates the logical progression of the PCM's temperature during the melting operation. The numerical model and the experimental results for the case reference have been matched. The considering data represent the temperature differences when the thermocouple nodes are installed at specific locations.
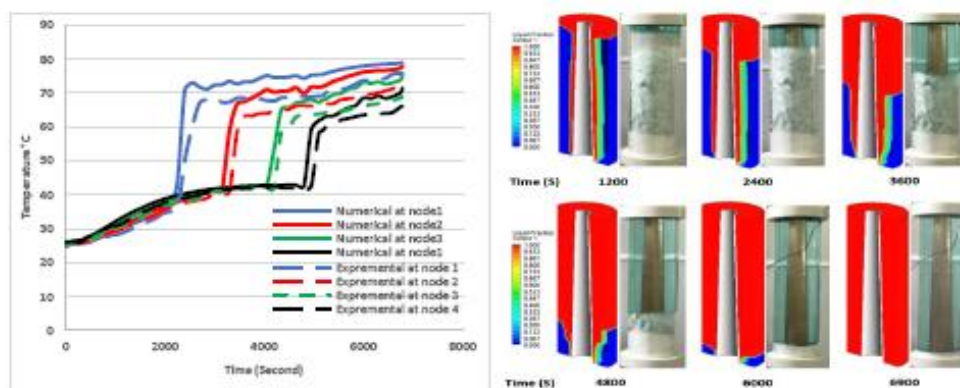

Figure 10:An evaluation patterns and behavers between the experimental data and numerical model for local PCM (lauric acid) temperatures at various nodes by thermocouples in a LHTES, at an input HTF temperature of 80°C and a mass flow rate of 7 L/min and the visualization validates at six designated time intervals.
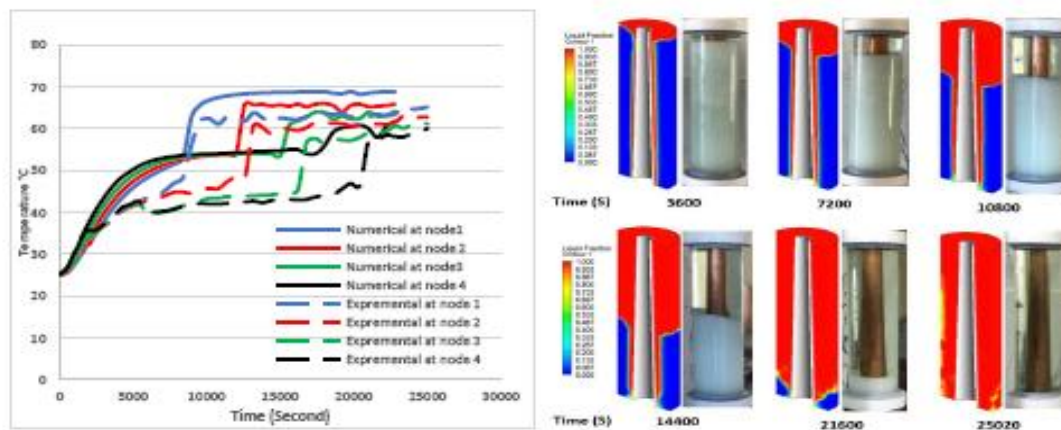

Figure 9:An evaluation patterns and behavers between the experimental data and numerical model for local PCM (Paraffin Wax) temperatures at various nodes by thermocouples in a LHTES, at an input HTF temperature of 70°C and a mass flow rate of 7 L/min and The visualization validates at six designated time intervals.

4.2-Effect melting point temperature (lauric acid and Paraffin wax):

Their melting point greatly influences PCMs' performance in the charging process. The melting point of PCM significantly impacts minimizing the time required for thermal charging operations in solar energy systems by utilizing lauric acid, such as PCM1, which has a melting point of about 9°C below that of paraffin wax, PCM 2. **Figure 11 (a,b and c)** illustrates the average distribution temperature and liquid fraction variations with time. As the rate of inlet temperature in the system is systematically increased, there is a significant acceleration in both the rate of temperature rise and the rate of melting. considering an inlet flow rate of 7 L/min and inlet temperatures of 70 °C, 75 °C, and 80 °C , respectively, decreases the melting time by using PCM1 about 62.33 %, 51.15 %, and 47.11 %, In comparison with PCM 2. Evidently, A positive correlation has been shown between a decrease in the melting point of PCMs and an increase in their melting time durations. as seen in Fig **12 d.** It also analyses the melting points at different percentages (0.2 -0.4- -0.6 - 0.8 -1) influence on the charging process and the extent to which it decreases the overall melting time of PCMs.
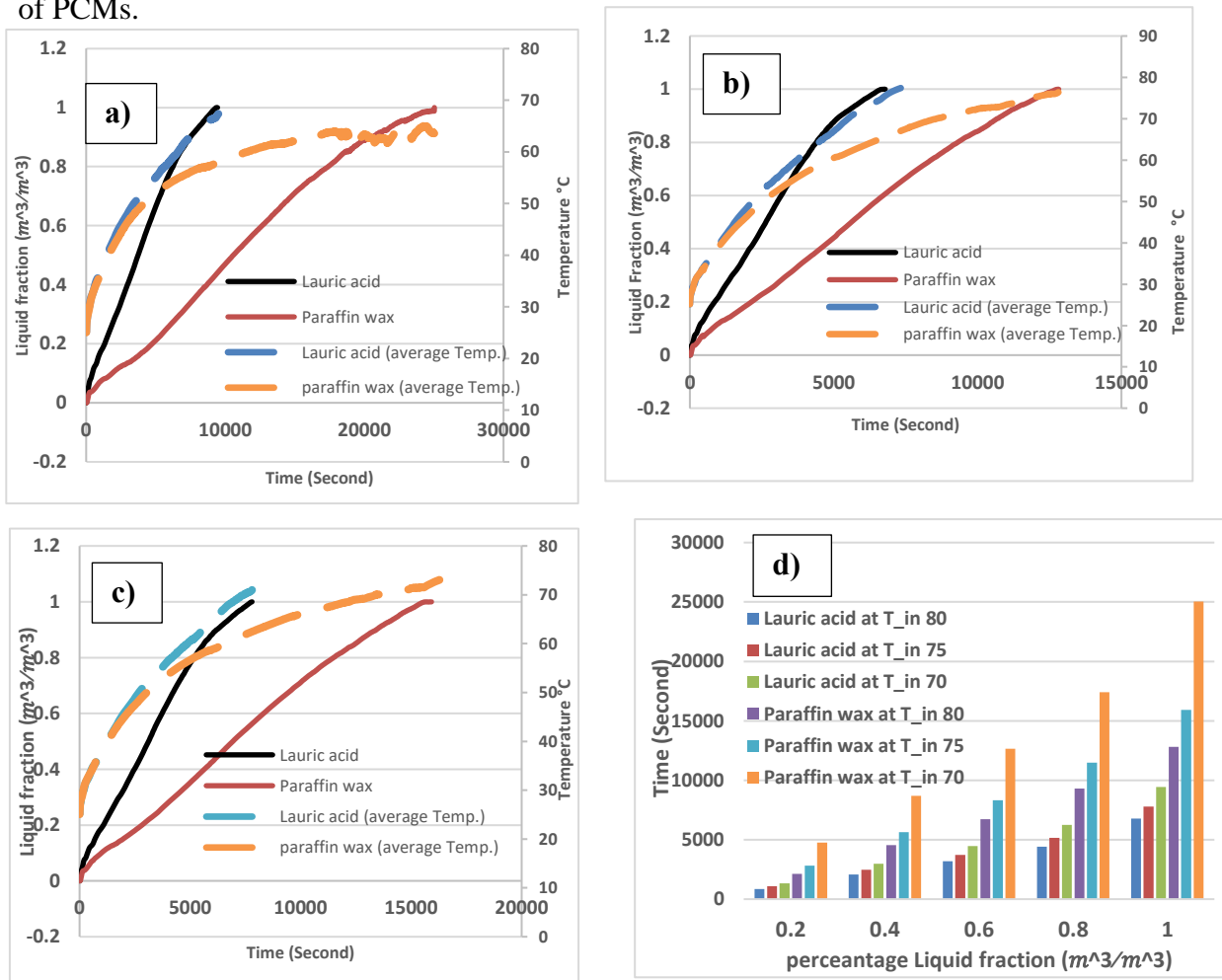

Figure. 11: Average liquid fraction and temperature of paraffin wax and lauric acid at various times with **a)** 70°C, **b)** 75°C, and **C)** 80°C inlet H.T.F temperature in case reference. **d)** A comparison of average liquid fraction percentage **(0.2, 0.4, 0.6 ,0.8and1)** vs. Time for various PCM (Paraffin wax and Lauric acid), at different T_{in}= (**70°C ,75°C and 80°C**)

4.3-Regions Melting in PCM

Following the charging period, the distribution temperature in various axial directions of LHSU is used to recognize the zones where the PCM becomes molten at different points in time. The temperature variations in PCM for all models and the total time of the melting cycle vary depending on the design. The numerical and empirical findings are obtained by measuring the inlet HTF temperature at 70°C and a flow rate of 7 LPM through the charging procedure. divides the melting in PCMs into three main domains. The first domain, called (sensible regions) occurs with the initiation of the charging procedure, specifically after the temperature reaches 25 °C, and finishes until PCM begins to melt, which occurs at approximately a temperature of 41.5°C.

The second (solid-liquid) domain begins until the exterior surface temperature of the PCM exceeds 43°C. Differences in the temperature of the PCM are capable of being identified depending on the positions of the prop during the path in the shell. In every situation, the temperature of the PCM jumps dramatically compared to that during the first domain due to the movement of the interface. The limits of this domain may be identified by the range of melting points for the PCM, which is between 44 °C- 58 °C.

The third domain is liquid PCM. The fusion of the PCM at the upper region of the testing section rises faster compared to the temperatures in both the central and bottom regions **Figure 12**. The rapid rise in the PCM's temperature in the region occurs when a thin layer of melted PCM appears surrounding the HTF tube surface. The molten layer is expected to shift due to the buoyancy-driven natural convection, resulting in a fast and finished melting process. Identical behaviors are also seen in the literature survey [38]and [43] The lowest temperature in the PCM is seen in the bottom region of the LHSU. As the procedure progresses, the melting begins at the highest point of the test unit and continues lower until it is completed
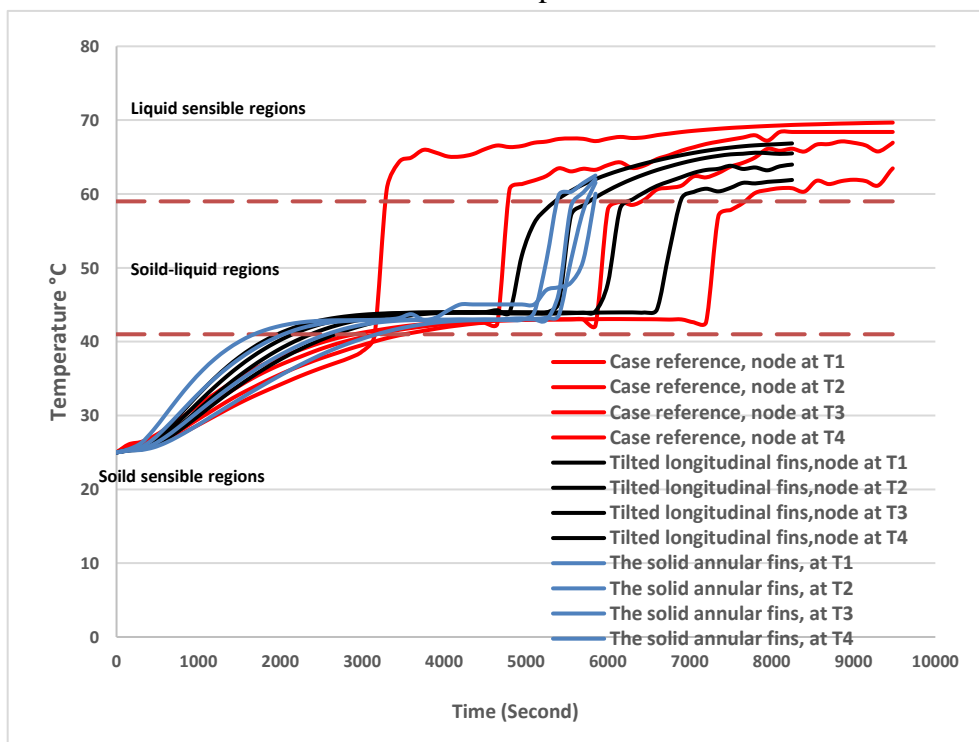

Figure 12: The patterns of the thermocouples during the lauric acid melting in LHTES with an HTF input temperature of 70 °C in all models.

4.4-Influence geometry parameters:

There are two different designs of fins, each with its individual arrangement, and the dimensions of the fins may change within each configuration. As mentioned previously, in models 2 and 3, the fins on the top shell side are reduced, while the fins on the bottom side are enlarged. According to **Figure 2b**, the Pattern dramatically speeds up the melting process on the bottom side. models 2 and 3 were initially intended to focus on peripheral regions along the inside boundary of the shell that showed less impact in the case reference. Conduction and free convection are the primary processes responsible for melting the PCM. The objective is to quickly liquefy the PCM briefly because the amount of powerful sunlight is limited. Hence, optimizing the design to facilitate the PCM quick melting is essential.

4.4.1-Case reference (model-1)

The modified converging tube increases the PCM's mass fraction and temperature compared to a straight tube. Consequently, the researchers' optimal conclusions about Korawan et al.2017 [46] Were adhered to, leading to the development of the thermal storage system. The convergent tube design is based on minimizing the surface areas exposed to natural convection currents. The hot liquid decreases in density and rises, resulting in a natural convection current on the top side, enhancing the melting rate in that area.

4.4.2-Tilted longitudinal fins (model-2)

Figure 13, the liquid fraction (interface) of the nozzle with tilted longitudinal fins is more extreme than that of the case reference. The variation is attributed to the second model, which increased the molten area compared to the case reference. **Figure 14** illustrate the fluctuation in countours temperature disterbustion for the specified configurations. The evidence clearly indicates that the liquid fraction in the second case (Tilted longitudinal fins) is considerably more significant than in the case reference during the first time period. **Figure 15** This demonstrates the second model's performance and the significance of integrating fins to augment the distribution of heat energy by employing conduction and convection techniques. Moreover, adding fins enhances the overall melting duration by approxi-mately 9.18 %, 5.25%, and 3.98%, which reduces it from 9370 s in the first case to 8510 s in this arrangement, from 7800 s in the second case, 7390 and minimized in third case 6790-6520, respectively.
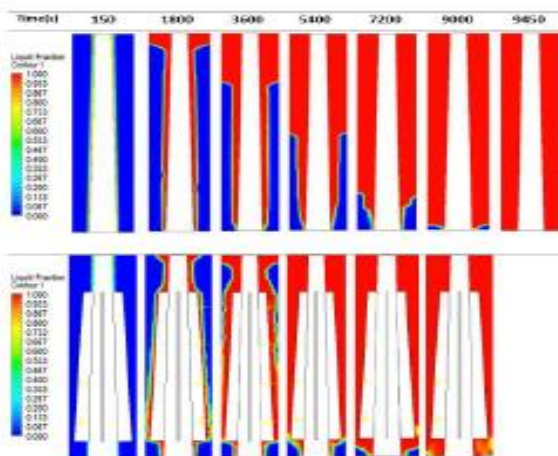

Figure 13: Contours of liquid fraction and for various cases of Tilted longitudinal fins compared to the case reference
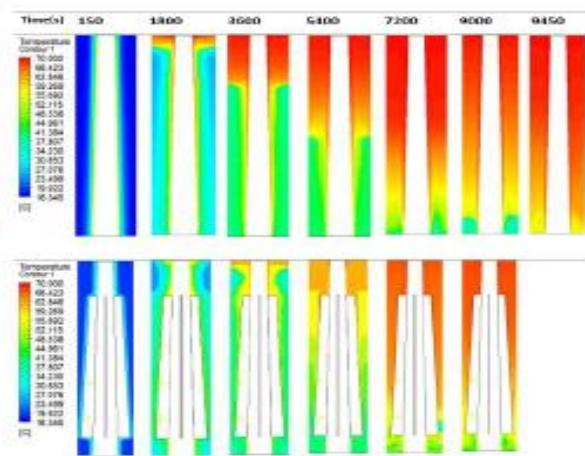
Figure 14: Contours of Temperature distributions for various cases of tilted longitudinal fins compared to the case reference.
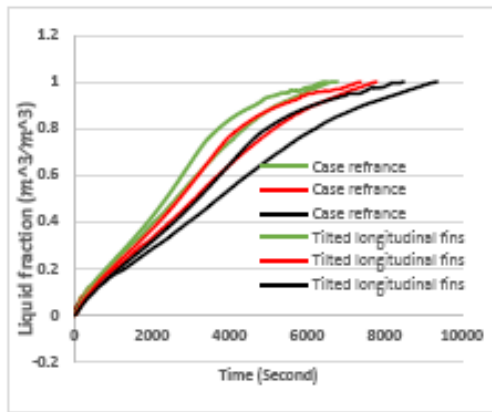
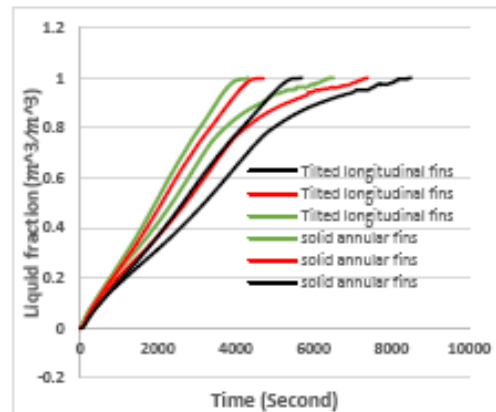Figure 15: The liquid fraction for various cases of tilted longitudinal fins compared to the case reference, Where T_{in}=70°C , 75°C,and 80°C

Figure 16: The liquid fraction for various cases the ten solid annular fins compared to the tilted longitudinal fins, Where T_{in}=70 °C , 75°C,and 80°C

4.4.3-The solid annular fins

The previous part demonstrated the high efficiency compared to the case reference. The fin configuration is not consistently effective. The bottom half of the shell retains parts that are less impacted as showin in **Figure 17 and 18**. New validation in this section presents the arrangement known as the model-3, The solid annular fins are located on the top side and have a relatively smaller diameter, whereas fins with large areas are concentrated on the underside of the shell. The design primarily focused on enhancing heat variation by conduction on the bottom side while reinforcing convection in the tiny gaps between the fins. Model 3 exhibits enhanced melting resulting from an optimized temperature distribution attributable to superior fin placement, while model 3 illustrates the most efficient design, achieving quick and virtually total melting within 5700 seconds.

Figures 5.16 compare the final melting times between the ten solid annular fins and tilted longitudinal fins, showing remarkable improvements. Case T_{in}=70 °C achieved a difference melting time of 2810 seconds (an improvement of 33.02%), T_{in}=75 °C at 2670 seconds (an improvement of 33.13%), and T_{in}=80 °C at 2200 seconds (an improvement of 33.74%). These results highlight the effectiveness of the ten solid annular fins in significantly enhancing the PCM's melting performance.
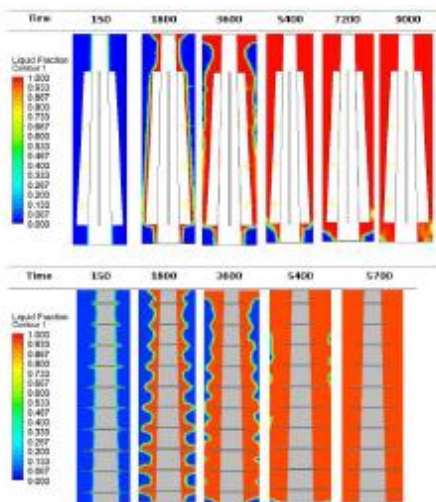

Figure 17: Contours of liquid fraction for various cases of the ten solid annular fins compared to the Tilted longitudinal fins.
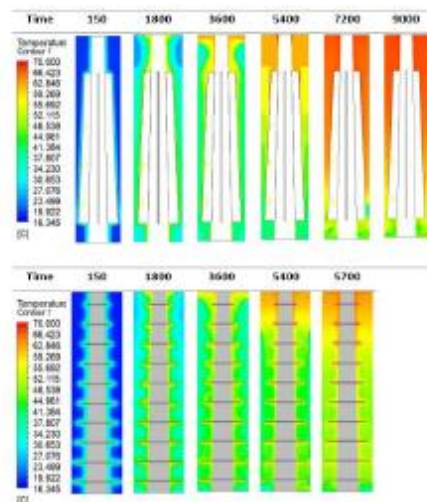
Figure 18: Contours of temperature distribution for various cases of the ten solid annular fins compared to the tilted longitudinal fins.

5.4-Inlet H.T.F temperature

Figure 19 shows the effects of HTF temperature on the average distribution of PCM temperatures in paraffin wax during the charging process. In the present investigation, several inlet HTF temperatures are examined to assess the influence of the T_{HTF} on the liquid fraction, ranging from 70°C to 80 °C, with a temperature increment of 5 °C in all In case reference with paraffin wax, the average temperature $T_{HTF,i}$ PCM in the LTESU increases consistently, but the overall melting time decreases. The enhancement in melting time was 34.97% and 21.32% when the inlet $T_{HTF,i}$ temp-erature was raised from 70-75°C and 75-80°C, respectively. **Figure 20** In the exact same case about inlet $T_{HTF,i}$ temperature but with lauric acid, the total time melting improved by (17.8%) & (8.72 %).

Furthermore, as the temperature of the HTF increases, the time disparities in the second model (Tilted longitudinal fins) progressively rise, as shown in **Figure 21.** Raising the input $T_{HTF,i}$ = 70°C-75°C and 75 °C-80 °C, the melting time was reduced by approximately 10.46 %, and by 10.67 %,the difference was minimized by (250 s- 190 s) and (930 -850) to achieve liquid fractions of 0.25 and 1 for three testings, respectively.

Moreover, as the temperature of the HTF increases in the third model (the solid annular fins), the time difference also rises, nevertheless maintaining the $T_{HTF,i}$ growth gradient constant at 5 °C, as shown in **Figure 22**. For instance, when the temperature rises from 70 °C - 75 °C and 75 °C -80°C, the enhancement in melting time is about 17.2 % and 7.84 %, while at the PCM liquid fraction percentage of 0.25, the average melting time difference is 300 and 90 seconds. The time difference for the complete liquid fraction percentage is 1 by 980 and 400 seconds, respectively.
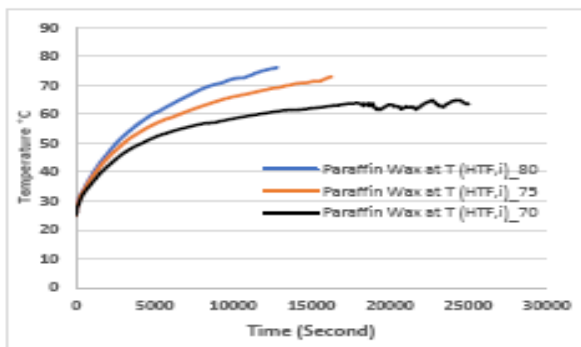

Figure 19: Time vs. dependent average temperature for case reference at $T_{HTF,i}$(70°C ,75°C, and 80°C) with Paraffin wax.
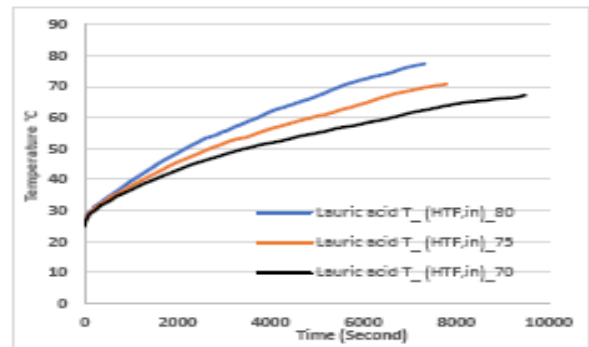

Figure 20: Time vs. dependent average temperature for case reference at $T_{HTF,i}$(70°C ,75°C, and 80°C) with Lauric acid.
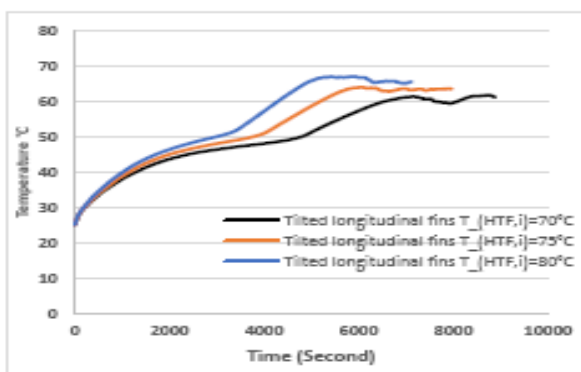

Figure 21: Time vs. dependent average temperature for tilted longitudinal fins at $T_{HTF,i}$(70°C ,75°C, and 80°C) with Lauric acid.
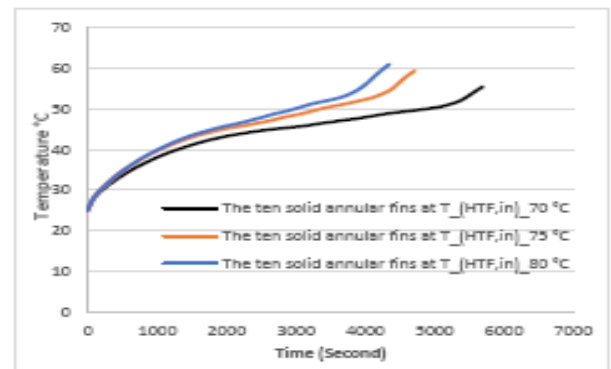

Figure 22: Time vs. dependent average temperature for the ten solid annular fins at $T_{HTF,i}$(70°C ,75°C, and 80°C) with Lauric acid.

5.5-Effect mass of HTF flow rate

An analysis is conducted to examine how the flow rate of HTF affects the performance of LTESU, specifically with respect to the instantaneous liquid fraction shown in **Figure 23.** The liquid fraction of PCM that is melted gradually rises until it reaches a value of one over time. Augmenting the mass flow rate reduces the total period required for complete melting. Nevertheless, the variation displayed in the computation results is very relatively minimal.

In addition, **Figure 24** provides the time necessary for PCM to achieve specific liquid fractions (0.25, 0.50, 0.75, and 1.0). The variation in time becomes more evident as the mass flow rate increases, but it keeps a similar liquid fraction percentage. For example, the time required to melt between 3 and 7 LPM differs by 180 seconds when the melting percentage is 0.25. However, it increases to 530 seconds for the complete melting. It indicates the maximum enhancement in total melting time was about 8.5 %. Based on the above data, raising the mass flow rate at the intake has a beneficial influence on the rate at which the PCM melts, but its influence is margin
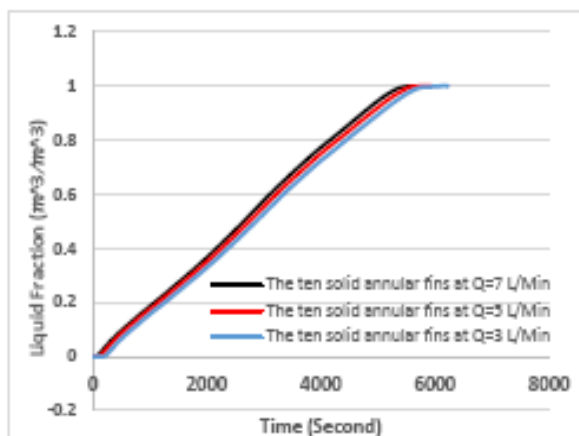

Figure 23: The liquid fraction vs. Time for the ten solid annular fins at various mass flow rates (3,5,7 L/Min) with Lauric acid.
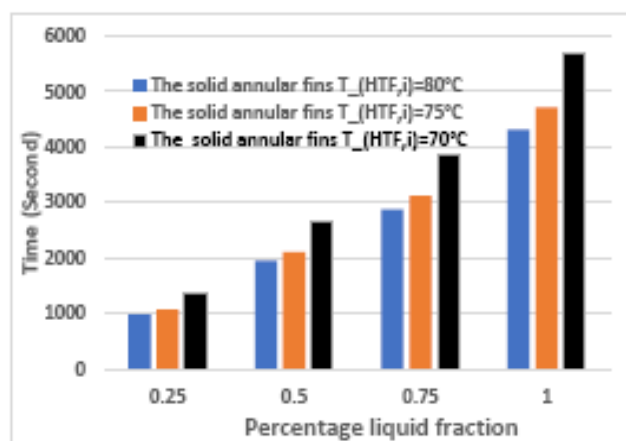
Figure 24: The average liquid fraction percentage (0.25,0.5, 0.75 and1) vs. Time for the ten solid annular fins at various mass flow rates (3,5, and 7 L/Min) with Lauric acid.

5.CONCLUSION

This work was examined the melting behavior of two commercial PCMs (lauric acid and paraffin wax) employed in three configurations: bare nozzle-finned and shell-and-nozzle (annular fins and tilted longitudinal fins) latent heat storage units and the influence of PCM thermal conductivity, inlet HTF temperature, inlet HTF flow rate. An experimental study was conducted to verify the numerical model. Upon validation of the numerical model, the thermal performance of the LHSUs was thoroughly examined using two indicators: complete melting time and temperature pattern distribution. The main results of this research may be summarized as follows:

PCM1 (lauric acid), which has a melting point of about 9°C below that of (paraffin wax), PCM 2. Considering an inlet flow rate of 7 L/min and inlet temperatures of 70 C, 75 C, and 80 C, respectively, decreases the melting time by using PCM1 about 62.33 %, 51.15 %, and 47.11 %, In comparison with PCM 2.

The enhancement is examined by comparing its performance parameters via those of a single nozzle tube and shell layout designated as (model-1) or case reference. Two fin geometries are under consideration: tilted longitudinal fins (model-2) and annular fins (model-3). The two models

are seen to speed up melting and provide time reductions of 12.98% and 38.3%, respectively, compared to the Case reference.

The overall melting time was enhanced by about 34.97% and 21.32% when the HTF's inlet temperature was increased from 70°C to 75°C and subsequently from 75°C to 80°C, respectively. In the exact same case with lauric acid, the total time melting improved by (17.8%) & (8.72 %). Furthermore, the inlet temperature of the HTF substantially affects the melting process in all geometric shapes, including tilted longitudinal fins with nozzle tubes. The decrease in melting time was 10.46 % and by 10.67 for the previously examined temperature ranges. The annular fins with nozzle tube LHSU exhibited percentage improvements of 17.2 % and 7.84 % when the inlet temperature of the HTF increased from 70°C to 75°C and subsequently from 75°C to 80°C, respectively. The relatively small convective thermal resistance on the HTF side during heat transfer results in a negligible impact of increased inlet HTF flow rate on the melting process.The largest increase in total melting time was around 8.5% when raising the flow rate from 3 to 7 L/Min, which indicates that raising the input HTF flow rate could be its influence is marginal.

REFERENCES

[1] J. P. O'Connor, "Modeling of atmospheric carbon dioxide (CO2) concentrations as a function of fossil-fuel and land-use change CO2 emissions coupled with oceanic and terrestrial sequestration," *Climate*, vol. 8, no. 5, 2020, doi: 10.3390/CLI8050061.

[2] R. Guchhait and B. Sarkar, "Increasing Growth of Renewable Energy: A State of Art," *Energies*, vol. 16, no. 6, p. 2665, Mar. 2023, doi: 10.3390/en16062665.

[3] I. Sarbu and C. Sebarchievici, "A comprehensive review of thermal energy storage," *Sustain.*, vol. 10, no. 1, 2018, doi: 10.3390/su10010191.

[4] B. Kalidasan, A. K. Pandey, S. Shahabuddin, M. Samykano, M. Thirugnanasambandam, and R. Saidur, "Phase change materials integrated solar thermal energy systems: Global trends and current practices in experimental approaches," *J. Energy Storage*, vol. 27, no. August 2019, p. 101118, 2020, doi: 10.1016/j.est.2019.101118.

[5] G. Dogkas, J. Konstantaras, M. K. Koukou, V. N. Stathopoulos, L. Coelho, and A. Rebola, "Evaluating a prototype compact thermal energy storage tank using paraffin-based phase change material for domestic hot water production," *E3S Web Conf.*, vol. 116, pp. 0–7, 2019, doi: 10.1051/e3sconf/201911600016.

[6] J. Guo, B. Zou, Y. Wang, and Y. Jiang, "Space heating performance of novel ventilated mortar blocks integrated with phase change material for floor heating," *Build. Environ.*, vol. 185, no. June, p. 107175, 2020, doi: 10.1016/j.buildenv.2020.107175.

[7] H. J. Akeiber, M. A. Wahid, H. M. Hussen, and A. T. Mohammad, "A newly composed paraffin encapsulated prototype roof structure for efficient thermal management in hot climate," *Energy*, vol. 104, pp. 99–106, 2016, doi: 10.1016/j.energy.2016.03.131.

[8] A. A. M. Omara and A. A. A. Abuelnour, "Improving the performance of air conditioning systems by using phase change materials: A review," *Int. J. Energy Res.*, vol. 43, no. 10, pp. 5175–5198, 2019, doi: 10.1002/er.4507.

[9] A. R. Abdulmunem and J. M. Jalil, "Indoor investigation and numerical analysis of PV cells temperature regulation using coupled PCM/Fins," *Int. J. Heat Technol.*, vol. 36, no. 4, pp. 1212–1222, 2018, doi: 10.18280/ijht.360408.

[10]   L. Kalapala and J. K. Devanuri, "Influence of operational and design parameters on the performance of a PCM based heat exchanger for thermal energy storage – A review," *J. Energy Storage*, vol. 20, no. September, pp. 497–519, 2018, doi: 10.1016/j.est.2018.10.024.

[11]   Q. Al-Yasiri and M. Szabó, "Paraffin As a Phase Change Material to Improve Building Performance: An Overview of Applications and Thermal Conductivity Enhancement Techniques," *Renew. Energy Environ. Sustain.*, vol. 6, no. October, p. 38, 2021, doi: 10.1051/rees/2021040.

[12]   R. Kumar and P. Verma, "An experimental and numerical study on effect of longitudinal finned tube eccentric configuration on melting behaviour of lauric acid in a horizontal tube-in-shell storage unit," *J. Energy Storage*, vol. 30, no. March, p. 101396, 2020, doi: 10.1016/j.est.2020.101396.

[13]   H. H. Kareem, F. M. Hussien, and J. J. Faraj, "The Numerical Simulation of Thermal Efficiency of Triple Pipe Heat Exchanger Using PCMs (Paraffin and Lauric Acid) System," *Int. J. Heat Technol.*, vol. 40, no. 6, pp. 1424–1431, 2022, doi: 10.18280/ijht.400609.

[14]   S. Seddegh, X. Wang, M. M. Joybari, and F. Haghighat, "Investigation of the effect of geometric and operating parameters on thermal behavior of vertical shell-and-tube latent heat energy storage systems," *Energy*, vol. 137, pp. 69–82, 2017, doi: 10.1016/j.energy.2017.07.014.

[15]   A. D. Korawan, S. Soeparman, W. Wijayanti, and D. Widhiyanuriyawan, "Increased Melting Heat Transfer in the Latent Heat Energy Storage from the Tube-and-Shell Model to the Combine-and-Shell Model," *Model. Simul. Eng.*, vol. 2017, 2017, doi: 10.1155/2017/8574184.

[16]   L. Wang *et al.*, "Unbalanced mass flow rate of packed bed thermal energy storage and its influence on the Joule-Brayton based Pumped Thermal Electricity Storage," *Energy Convers. Manag.*, vol. 185, no. December 2018, pp. 593–602, 2019, doi: 10.1016/j.enconman.2019.02.022.

[17]   B. Lu, Y. Zhang, D. Sun, Z. Yuan, and S. Yang, "Experimental investigation on thermal behavior of paraffin in a vertical shell and spiral fin tube latent heat thermal energy storage unit," *Appl. Therm. Eng.*, vol. 187, no. September 2020, p. 116575, 2021, doi: 10.1016/j.applthermaleng.2021.116575.

[18]   V. Safari, H. Abolghasemi, L. Darvishvand, and B. Kamkari, "Thermal performance investigation of concentric and eccentric shell and tube heat exchangers with different fin configurations containing phase change material," *J. Energy Storage*, vol. 37, no. February, p. 102458, 2021, doi: 10.1016/j.est.2021.102458.

[19]   M. A. Kibria, M. R. Anisur, M. H. Mahfuz, R. Saidur, and I. H. S. C. Metselaar, "Numerical and experimental investigation of heat transfer in a shell and tube thermal energy storage system," *Int. Commun. Heat Mass Transf.*, vol. 53, pp. 71–78, 2014, doi: 10.1016/j.icheatmasstransfer.2014.02.023.

[20]   M. Eslami, F. Khosravi, and H. R. Fallah Kohan, "Effects of fin parameters on performance of latent heat thermal energy storage systems: A comprehensive review," *Sustain. Energy Technol. Assessments*, vol. 47, no. May 2020, p. 101449, 2021, doi: 10.1016/j.seta.2021.101449.

[21]   J. M. Mahdi, H. I. Mohammed, E. T. Hashim, P. Talebizadehsardari, and E. C. Nsofor,

"Solidification enhancement with multiple PCMs, cascaded metal foam and nanoparticles in the shell-and-tube energy storage system," *Appl. Energy*, vol. 257, no. September 2019, p. 113993, 2020, doi: 10.1016/j.apenergy.2019.113993.

[22]   S. L. Tariq, H. M. Ali, M. A. Akram, M. M. Janjua, and M. Ahmadlouydarab, "Nanoparticles enhanced phase change materials (NePCMs)-A recent review," *Appl. Therm. Eng.*, vol. 176, no. April, p. 115305, 2020, doi: 10.1016/j.applthermaleng.2020.115305.

[23]   X. Yang, P. Wei, X. Wang, and Y. L. He, "Gradient design of pore parameters on the melting process in a thermal energy storage unit filled with open-cell metal foam," *Appl. Energy*, vol. 268, no. April, p. 115019, 2020, doi: 10.1016/j.apenergy.2020.115019.

[24]   M. M. Heyhat, S. Mousavi, and M. Siavashi, "Battery thermal management with thermal energy storage composites of PCM, metal foam, fin and nanoparticle," *J. Energy Storage*, vol. 28, no. December 2019, p. 101235, 2020, doi: 10.1016/j.est.2020.101235.

[25]   B. Buonomo, O. Manca, S. Nardini, R. E. Plomitallo, D. Ingegneria, and C. Luigi, "Numerical Investigation on Shell and Tube Latent Heat Thermal Energy Storage with External Heat Losses Partially Filled with Metal Foam," vol. 40, no. 4, pp. 895–900, 2022.

[26]   X. Yang, Z. Niu, Q. Bai, H. Li, X. Cui, and Y. L. He, "Experimental study on the solidification process of fluid saturated in fin-foam composites for cold storage," *Appl. Therm. Eng.*, vol. 161, no. January, p. 114163, 2019, doi: 10.1016/j.applthermaleng.2019.114163.

[27]   H. Li, C. Hu, Y. He, D. Tang, and K. Wang, "Influence of fin parameters on the melting behavior in a horizontal shell-and-tube latent heat storage unit with longitudinal fins," *J. Energy Storage*, vol. 34, no. December 2020, p. 102230, 2021, doi: 10.1016/j.est.2020.102230.

[28]   X. Yang, Z. Lu, Q. Bai, Q. Zhang, L. Jin, and J. Yan, "Thermal performance of a shell-and-tube latent heat thermal energy storage unit: Role of annular fins," *Appl. Energy*, vol. 202, pp. 558–570, 2017, doi: 10.1016/j.apenergy.2017.05.007.

[29]   J. Duan, Y. Xiong, and D. Yang, "Study on the effect of multiple spiral fins for improved phase change process," *Appl. Therm. Eng.*, vol. 169, no. August 2019, p. 114966, 2020, doi: 10.1016/j.applthermaleng.2020.114966.

[30]   S. Pakalka, K. Valančius, and G. Streckienė, "Experimental comparison of the operation of PCM-based copper heat exchangers with different configurations," *Appl. Therm. Eng.*, vol. 172, no. December 2019, 2020, doi: 10.1016/j.applthermaleng.2020.115138.

[31]   Y. Huang, F. Yao, and X. Liu, "Numerical study on the thermal enhancement of horizontal latent heat storage units with hierarchical fins," *Renew. Energy*, vol. 180, pp. 383–397, 2021, doi: 10.1016/j.renene.2021.08.100.

[32]   L. Wu, X. Zhang, and X. Liu, "Numerical analysis and improvement of the thermal performance in a latent heat thermal energy storage device with spiderweb-like fins," *J. Energy Storage*, vol. 32, no. May, p. 101768, 2020, doi: 10.1016/j.est.2020.101768.

[33]   Y. Tian *et al.*, "Bionic topology optimization of fins for rapid latent heat thermal energy storage," *Appl. Therm. Eng.*, vol. 194, no. May, p. 117104, 2021, doi: 10.1016/j.applthermaleng.2021.117104.

[34]   V. Safari, H. Abolghasemi, and B. Kamkari, "Experimental and numerical investigations of thermal performance enhancement in a latent heat storage heat exchanger using bifurcated and straight fins," *Renew. Energy*, vol. 174, pp. 102–121, 2021, doi: 10.1016/j.renene.2021.04.076.

[35]   A. K. Hassan, J. Abdulateef, M. S. Mahdi, and A. F. Hasan, "Experimental evaluation of thermal performance of two different finned latent heat storage systems," *Case Stud. Therm. Eng.*, vol. 21, 2020, doi: 10.1016/j.csite.2020.100675.

[36]   X. Yang, J. Guo, B. Yang, H. Cheng, P. Wei, and Y. L. He, "Design of non-uniformly distributed annular fins for a shell-and-tube thermal energy storage unit," *Appl. Energy*, vol. 279, no. July, p. 115772, 2020, doi: 10.1016/j.apenergy.2020.115772.

[37]   S. Tiari, A. Hockins, and M. Mahdavi, "Numerical study of a latent heat thermal energy storage system enhanced by varying fin configurations," *Case Stud. Therm. Eng.*, vol. 25, no. November 2020, p. 100999, 2021, doi: 10.1016/j.csite.2021.100999.

[38]   R. Karami and B. Kamkari, "Experimental investigation of the effect of perforated fins on thermal performance enhancement of vertical shell and tube latent heat energy storage systems," *Energy Convers. Manag.*, vol. 210, no. November 2019, p. 112679, 2020, doi: 10.1016/j.enconman.2020.112679.

[39]   L. Pu, S. Zhang, L. Xu, and Y. Li, "Thermal performance optimization and evaluation of a radial finned shell-and-tube latent heat thermal energy storage unit," *Appl. Therm. Eng.*, vol. 166, p. 114753, 2020, doi: 10.1016/j.applthermaleng.2019.114753.

[40]   R. Dai, X. Lu, X. Tong, and J. Deng, "Thermal performance analysis of different T-shaped fin configurations on thermal energy storage through simplified enthalpy based lattice Boltzmann method," *Case Stud. Therm. Eng.*, vol. 53, no. November 2023, p. 103861, 2024, doi: 10.1016/j.csite.2023.103861.

[41]   A. H. N. Al-Mudhafar, A. F. Nowakowski, and F. C. G. A. Nicolleau, "Enhancing the thermal performance of PCM in a shell and tube latent heat energy storage system by utilizing innovative fins," *Energy Reports*, vol. 7, pp. 120–126, 2021, doi: 10.1016/j.egyr.2021.02.034.

[42]   L. A. Khan and M. M. Khan, "Role of orientation of fins in performance enhancement of a latent thermal energy storage unit," *Appl. Therm. Eng.*, vol. 175, no. April, p. 115408, 2020, doi: 10.1016/j.applthermaleng.2020.115408.

[43]   M. S. Mahdi *et al.*, "Numerical study and experimental validation of the effects of orientation and configuration on melting in a latent heat thermal storage unit," *J. Energy Storage*, vol. 23, no. April, pp. 456–468, 2019, doi: 10.1016/j.est.2019.04.013.

[44]   F. Benmoussa, A. Benzaoui, and H. Benmoussa, "Thermal behavior of latent thermal energy storage unit using two phase change materials: Effects of HTF inlet temperature," *Case Stud. Therm. Eng.*, vol. 10, no. August, pp. 475–483, 2017, doi: 10.1016/j.csite.2017.10.010.

[45]   N. Zhang, Z. Huang, X. Wang, and B. Zheng, "Combustion and emission characteristics of a turbo-charged common rail diesel engine fuelled with diesel-biodiesel-DEE blends," *Front. Energy Power Eng. China*, vol. 5, no. 1, pp. 104–114, 2011, doi: 10.1007/s11708-011-0138-x.

[46]   A. D. Korawan, S. Soeparman, W. Wijayanti, and D. Widhiyanuriyawan, "3D numerical and experimental study on paraffin wax melting in thermal storage for the nozzle-and-shell, tube-and-shell, and reducer-and-shell models," *Model. Simul. Eng.*, vol. 2017, no. April, p. 9, 2017, doi: 10.1155/2017/9590214.